RSC Advances

PAPER

Cite this: *RSC Adv.*, 2022, **12**, 19571

Shape controlled synthesis of concave octahedral Au@AuAg nanoparticles to improve their surface-enhanced Raman scattering performance†

Cuixia Bi, *[a] Yahui Song,[b] Hongyan Zhao[a] and Guangqiang Liu*[a]

Received 26th April 2022
Accepted 30th June 2022

DOI: 10.1039/d2ra02651a

rsc.li/rsc-advances

In this work, a seed mediated strategy has been proposed to design and fabricate uniform octahedral shaped gold@gold-silver nanoparticles (Au@AuAg NPs) with unique concave structure and an AuAg alloy shell. The morphology and Au/Ag ratio of the Au@AuAg nanostructures can be delicately controlled by varying the concentration of reagents, namely the Au nanorod (NR) seeds, $HAuCl_4$ and $AgNO_3$ precursor. Besides, the investigation of the growth mechanism revealed that the morphology of the product also can be controlled by tuning the growth time. Furthermore, uniformly arranged assemblies of concave octahedral Au@AuAg NPs were prepared through a solvent evaporation self-assembly strategy and employed as surface-enhanced Raman scattering (SERS) substrates, effectively applied to the analysis of R6G for the examination of SERS performance. Satisfyingly, owing to the synergistic effect between the Au and Ag elements and concave structure, concave octahedral Au@AuAg NPs exhibit significantly higher SERS enhancement compared with traditional octahedral Au NPs, which have an enhancement factor of $\sim 1.3 \times 10^7$ and a detection limit as low as 10^{-10} M. Meanwhile, the SERS substrate reveals an excellent uniformity and reproducibility of the SERS performance. This work opens a new avenue toward bimetallic NPs with concave structure, which have broad application prospects in optics, SERS detection and other fields.

1. Introduction

Metal nanoparticles (NPs) with well-defined and controllable shapes have attracted tremendous attention owing to their extraordinary optical properties. Among various metal NPs, Au and Ag NPs have been extensively researched and found widespread applications based on their unique surface plasmon resonance (SPR) property, such as optical labeling, biological sensing, and surface enhanced Raman scattering (SERS).[1–6] SERS is recognized as a simple, rapid and ultrasensitive spectroscopic analytical tool for the fields of biochemical analysis,[7,8] environment testing,[9,10] and trace detection of organic chemicals.[11,12] The SERS signals can be enhanced by electromagnetic hotspots derived from sharp structures (tips, edges and corners) and nanogaps (intergaps between adjacent NPs and intragaps within a NP).[13–15] An ideal SERS substrate should have excellent characteristics such as high sensitivity, chemical stability, spatial uniformity and reproducibility. In general, Ag NPs exhibit superior plasmonic response, strong local field electromagnetic enhancement, high sensitivity towards physical and chemical changes in their surrounding environment that led to high SERS properties in SERS applications.[14,16,17] However, Ag NPs are unstable as they susceptibility to oxidation that usually easy to cause changes in morphology, thereby leading a low durability and reproducibility in their practical applications.[18] Correspondingly, Au NPs have excellent chemical resistance, easy surface modification and good biocompatibility, but the sensitivity is at least one order of magnitude lower than that of Ag NPs.[19,20] In this context, Au–Ag bimetallic NPs have received considerable attention owing to their particular physicochemical properties, derived from the synergistic effect between these two elements will combine the properties of the constituent materials. Hence, Au–Ag bimetallic nanomaterials intend to overcome the instability of Ag NPs while keep the advantage of its higher enhancement effect.[21,22]

In addition, the properties of the AuAg bimetallic NPs also largely depend on the morphology and size, thus, their

[a]*School of Physics and Physical Engineering, Qufu Normal University, Qufu, 273165, P. R. China. E-mail: cxbi@qfnu.edu.cn; gqliu@qfnu.edu.cn*

[b]*Academy of Advanced Interdisciplinary Studies, Qilu University of Technology, Jinan, 250000, P. R. China*

† Electronic supplementary information (ESI) available: TEM image and corresponding geometric models of concave octahedral Au@AuAg, TEM images of an individual concaved octahedral Au@AuAg NP at different tilting angles, TEM images and UV-vis spectra of NPs synthesized at different CTAC concentrations, EDS spectrum of Au@AuAg NPs, XRD patterns of concave octahedral Au@AuAg NPs, digital photos and SEM images of the self-assembled concave octahedral Au@AuAg NPs, TEM images and UV-vis spectra of octahedral Au NPs and Ag NPs, Raman spectra of R6G molecules, atomic ratio of Au and Ag of the NPs synthesized at different $HAuCl_4$ and $AgNO_3$ concentrations. See https://doi.org/10.1039/d2ra02651a

controllable preparation is essential for regulating their physicochemical properties and achieving better applications. To date, significant methods have been explored for the preparation of Au–Ag NPs with controllable morphologies. For example, Meng and co-workers have successfully prepared spiky Au@Ag core–shell NPs with controlled Au core size and Ag shell thickness, which provide excellent SERS activities for p-ATP, and the average enhancement factor (EF) value was 1.2×10^6 for spiky Au_{133nm} NPs and 6.7×10^7 for spiky $Au_{133nm}@Ag_{2nm}$ core–shell NPs.[23] Qin *et al.* synthesised Ag@Au–Ag concave nanocrystals as SRES substrate, which exhibit much stronger SERS activity than that of Ag nanocubes.[24] Liu *et al.* have successfully synthesized three kinds of plasmonic mesoporous AuAg (mesoAuAg) nanopheres, including well-alloyed mesoAuAg, core–shell Ag-mesoAu, and hollow mesoAuAg nanospheres.[25] And several other types of Au–Ag bimetallic NPs with different morphologies have been synthesized, such as, Au@AgAu yolk–shell nanorods,[26] cornlike bimetallic Au/Ag core–shell superstructures.[27] In particular, NPs with concave structure reveal certain novel characteristics such as sharp edges/corners, surface cavity, and negative curvature, which make it show special structural advantages in optics, catalysis, SERS, *etc.* This is because the concave surface has a more open atomic arrangement, which can provide more active site, and the sharp feature of the edges and corners could enhance the local plasma resonance effect. Important progresses have recently been made in the preparation of metal NPs with concave structure, for instance, concave cubic Au NPs, concave cuboid Au NPs and concave octahedral Ag NPs have been successfully prepared.[28–30] However, as the formation of concave surface with negative curvature is thermodynamically unfavourable and requires significantly more energy, synthesis of such structure remains a major challenge.[31–33] There have been very few reports on the concave octahedral structure of Au@AuAg NPs, as most of the previous researches focused on the pure Au and Ag NPs with concave structure. Combining the above-mentioned properties, we rational designed and successfully synthesized concave octahedral Au@AuAg NPs with both AuAg alloy shells and concave structure.

Herein, we demonstrate a modified seed-mediated growth method to prepare uniform concave octahedral Au@AuAg NPs with well-defined morphology and AuAg alloy shell by co-reducing Au and Ag precursors into Au NRs using AA and CTAC as reducing agent and surfactant, which combined both the excellent plasmonic activity of Ag and the high stability of Au. Their intrinsic properties derived from the synergistic effects of Ag and Au, thus outperforming similar nanostructures with monometallic shells. The structure has a unique concave structure, which can provide a large number of concave surfaces and sharp edges and corners. The local electric field intensity of concave octahedral Au@AuAg NPs is significantly enhanced among or between concave faces as well as the corners and edges, affording more hotspots to promote their application in SERS.[34–36] Notwithstanding, the random distribution of hotspots on substrates leads to poor uniformity and reproducibility of SERS measurements, which greatly limiting their practical application. Therefore, its desirable to fabricate uniform ensembles with high-density hotspots through reasonable design the geometric arrangement of NPs to further improve SERS performance in practical application. Then, the synthesized concave octahedral Au@AuAg NPs were assembly into an orderly array *via* a simple bulk solvent evaporation self-assembly strategy and used as SERS substrate to investigate SERS performance. Thanks to the synergistic effect of Au and Ag elements, sharp corners/edges, and high-density hotspots in nanogaps, such concave octahedral Au@AuAg NPs showed excellent SERS performance. Additionally, highly homogeneous concave octahedral Au@AuAg NPs ordered array would significantly enhance the uniformity and reproducibility of the SERS performance, which is of great significance for potential SERS practical application.

2. Experimental section

2.1 Materials

Hydrogen tetrachloroaurate tetrahydrate ($HAuCl_4 \cdot 4H_2O$), Cetyltrimethylammonium bromide (CTAB), Cetyltrimethylammonium chloride (CTAC), sodium borohydride ($NaBH_4$), and L-ascorbic acid (AA) were purchased from Sinopharm. Chemical Reagent Co., Ltd. Silver nitrate ($AgNO_3$) was purchased from Alfa. Rhodamine 6G (R6G) was purchased from Sigma-Aldrich. Milli-Q deionized water with a resistivity higher than 18.2 MΩ cm^{-1} were used for all experiments.

2.2 Synthesis of Au NRs

First, the Au NRs were prepared by the seed-mediated growth method according to a previously proposed approach with some modifications.[37,38] Briefly, $NaBH_4$ (0.01 M, 0.6 mL) was added into a mixture of CTAB (0.1 M, 7.5 mL) and $HAuCl_4$ (0.025 M, 100 μL). The seed solution was left at 28 °C for 2 h. The synthesis procedure of Au NRs was as follows. The growth solution was perpared by mixing CTAB (0.1 M, 20 mL), $HAuCl_4$ (0.025 M, 320 μL), $AgNO_3$(0.01 M, 120 μL). Afterward, 90 μL of 0.1 M AA and 240 μL of the seed solution were successively added to the aforementioned growth solution under vigorous stirring. After 30 s, the resulting mixture was left at 28 °C and aged for 3 h. The obtained Au NRs were washed with ultrapure water for two times by centrifugation (8000 rcf, 8 min) and redispersed in 2.5 mL of 0.1 M CTAB solution for further use.

2.3 Preparation of concave octahedral Au@AuAg NPs

High quality concave octahedral Au@AuAg NPs can be repeatedly and reproducibly prepared in presence of CTAC. In a typical synthesis of the concave octahedral Au@AuAg NPs, the growth solution consisting CTAC (0.1 M, 2 mL), H_2O (3.6 mL), $HAuCl_4$ (0.025 M, 60 μL) and, $AgNO_3$ (0.01 M, 60 μL) was added to 10 mL conical flasks. Afterward, 90 μL of 0.10 M AA was quickly added to the aforementioned growth solution, which resulted in the mixture solution immediately change from light yellow to colorless. Then, the as-prepared Au NR seeds solution (enrichment 8 times, 0.3 mL) was quickly injected to the above mixture with moderate stirring. After further stirring for 5 min the flask was transferred to a 28 °C water bath for 6 h, yielding concave

octahedral Au@AuAg NPs with good uniformity and reproducibility. The obtained concave octahedral Au@AuAg NPs were collected and washed with ultrapure water twice through centrifugation cycles (at 8000 rcf for 8 min).

2.4 Self-assembly of concave octahedral Au@AuAg NPs

The controlled self-assembly of concave octahedral Au@AuAg NPs was realized by using a bulk solution evaporation method.[39] The clean glass circular sheet (~6 mm in diameter and 0.5 mm in thickness) was flatly placed at the bottom of one vessel (~6.5 mm in inner diameter) of a plastic 96-well tissue culture plate. Specifically, glass substrates were cleaned in ethanol and ultrapure water, respectively, followed by plasma clean the surfaces. Subsequently, 0.3 mL of centrifugally concentrated concave octahedral Au@AuAg NPs dispersion was injected into the vessel. The vessel was covered by a piece of filter paper and vial sealed with the lid in order to reduce the evaporation rate of the solvent. The 96-well tissue culture plate was kept undisturbed for a week at room tempureature until the completion of evaporation. Then, a gold-colored film with ~6 mm diameter was formed on the glass plates base. The dry glass plates with concave octahedral Au@AuAg NPs was then immersed successively in chloroform and water for 30 min to wash away the free surfactants.

2.5 Characterization

Transmission electron microscopy (TEM) and Scanning electron microscopy (SEM) images were obtained with a JEOL JEM 2100F TEM at an acceleration voltage of 200 kV and a Carl Zeiss AG instrument (Sigma 500 VP) at an acceleration voltage of 5 kV. High-angle annular dark-field scanning transmission electron microscopy (HAADF-STEM) and elemental mapping images were acquired by energy dispersive X-ray spectroscopy (EDS) using a JEOL JEM-2100F electron microscope equipped with a STEM unit. All UV-vis extinction spectroscopy were obtained using a Cary 50 spectrophotometer. X-ray diffraction (XRD) patterns of the as-prepared samples were collected with a PANalytical X-ray Diffractometer Model X pert3 with Cu $K\alpha$ radiation using a graphite monochromator. Diffraction peaks were recorded in the 30°–90°(2θ) range with a step size of 0.02°.

2.6 SERS measurements

For the SERS enhancements test, the glass plates with concave octahedral Au@AuAg NPs were first plasma-treated for 5 min and then submerged into a freshly prepared 5 mL ethanol solution of Rhodamine 6G (R6G) for at least 2 h. The concentrations of R6G used in our work were in the range of 10^{-4}–10^{-10} M. Then the samples were thoroughly washed with ethanol to remove extra molecules. The samples were then taken out and thoroughly rinsed with ethanol to remove unbound molecules and dried in a N_2 stream. Raman spectra were recorded at room temperature using a Horiba LabRAM HR Evolution spectrograph with an excitation wavelength of 633 nm. The laser power was 0.2 mW and the exposition time was 10 s.

3. Results and discussion

3.1 Synthesis of concave octahedral Au@AuAg NPs

Fig. 1a schematically shows the structural transformation from a Au NR to an arrow shaped NP, and the subsequent transformation into a concave octahedral Au@AuAg NP *via* a seed-mediated growth method. Single-crystalline Au NRs (seeds in Fig. 1c) with an average length of 43 nm and an average diameter of 12 nm, were synthesized according to a modified seed-mediated growth process containing CTAB surfactant and Ag+ ions mixtures. The Au NRs were utilized as the seeds for another round of growth to generate concave octahedral Au@AuAg NPs, through introduced them into a growth solution containing CTAC, AA, $HAuCl_4$ and $AgNO_3$ precursor, and then allowed to grow. In order to investigate the growth mechanism of concave octahedral Au@AuAg NPs, we followed their growth over time by taking out certain amounts of growth solution at specified time periods for UV-vis spectroscopy analysis and centrifuged to stop the reaction for TEM measurements (Fig. 1c and d). Fig. 1b show the time-dependent UV-vis spectroscopy measurement during the growth of the concave octahedral Au@AuAg NPs at 0 s, 10 s, 30 s, 1 min, 3 min, 5 min, 10 min, 15 min, 30 min, 1 h, 6 h, and 12 h, respectively. The UV-vis spectra of the original Au NR dispersion display a longitudinal SPR (L-SPR) peak centered at 714 nm and a weak transverse SPR (T-SPR) peak at 512 nm (black line in Fig. 1b). During the growth process, after the addition of Au NRs for 10 s, the L-SPR peaks experience a considerably blue-shift of 29 nm from 714 to 685 nm attributed to the decreasing aspect ratio, indicating the increment in transverse faster than the longitudinal at initial stage of Au NRs. This is complemented by the TEM images (Fig. 1c and d) which clear show structures transformation from cylindrical Au NRs into arrow-headed NPs, seems that Au and Ag atoms preferably deposit on the plane of ends. With the proceeding of the reaction, the UV-vis spectra showed the L-SPR continuously blue-shift from 685 to 553 nm, while the T-SPR slightly red-shift from 515 to 527 nm (Fig. 1b). Synchronously, the intensities

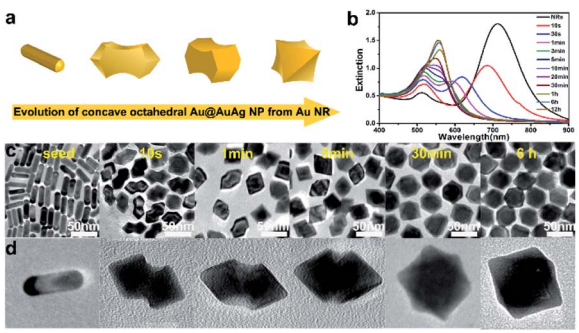

Fig. 1 Schematic illustration of possible formation process of concave octahedral Au@AuAg NPs (a). Temporal evolution of the UV-vis spectra (b) of the reaction solution recorded at different reaction time: 0, 10 s, 30 s, 1 min, 3 min, 5 min, 10 min, 20 min, 30 min, 1 h, 6 h, and 12 h, respectively, and corresponding TEM images (c and d) of intermediate products taken from the solutions: 0 (seeds), 10 s, 1 min, 5 min, 30 min, and 6 h respectively.

of the L-SPR peak is gradually weakened and the T-SPR is significantly enhanced. Then, the L-SPR and T-SPR peaks merged into a single peak after reaction about 15 min and finally located at the position of 560 nm. The SPR peak eventually red-shifted as well as narrowed attributed to the growth and homogenization of the resultant concave octahedral Au@AuAg NPs. Time-dependent morphological evolution of the concave octahedral Au@AuAg NPs shows that two small swelling heads were formed on both ends of the Au NRs initially and the center begins to grow accompanying the formation of the concave structure, which quickly developed into concave octahedral Au@AuAg NPs with surface cavity in 30 min. The NPs growth reached an equilibrium state after 6 h, well-developed concave octahedral Au NPs with both high yield and good uniformity were obtained, and basically essentially remained unchanged after a prolonged period of time which was also reflected in the UV-vis spectra without obvious peak shifting. The observed results strongly suggest that arrow-head NPs were formed as intermediates during the growth and the morphology of concave octahedral Au@AuAg NPs can be controlled by adjusting the reaction time.

It is worth noting that the shape of concave octahedral Au@AuAg NPs displayed in TEM images is diverse because of the NP orientated along different directions (Fig. S1†). To fully characterize the structure of the concaved octahedron, a set of TEM images of an individual concaved octahedral Au@AuAg NP was recorded at different tilting angles with x as the rotation axis from -50° to 60° at intervals of 10° (Fig. S2†). From the rotation image of a single NP, we can clearly see that the projection images of one NP displayed different angles are significantly various, which also proves why there are different shapes of NPs in the above TEM image. Furthermore, the light and dark portions correspond to the middle region and the protruded edges of the selected individual concaved octahedral Au@AuAg NP correspond to the thick middle part and thin protruded edge, which further proves the formation of concave structure on the surface and each side face of the octahedron being excavated by a curved cavity in the center.

As the concentration of seed plays a vital role in the control of NP growth, the Au NR seed volumes was systematically reduced from 900 to 600, 450, 300 and 100 μL, while all the reaction conditions were kept constant in the reaction medium. The morphology of the obtained products can be readily adjusted by changing the Au NR seed volumes to control the overgrowth process of Au NR (Fig. 2). It can be observed that at higher Au NR volume (900 μL) the obtained NPs with an arrow-head shape (Fig. 2a). As the Au NR volume was decreased to 600 μL, maintain an arrow-head shape but with the two pyramidal heads gradually grew larger and closer, whereas their length stayed almost constant and the diameter increased, leading to a lower aspect ratio (Fig. 2b). Upon further decreased Au NR solution to 400 μL, spindle morphology NPs were obtained and appeared by a few concave octahedral NPs, and a slightly lower aspect ratio (Fig. 2c). When 300 μL Au NR seeds were used, the NPs become ideal concave octahedrons with a smaller aspect ratio (Fig. 2d). Finally, the Au NR volume decreased to 100 μL,

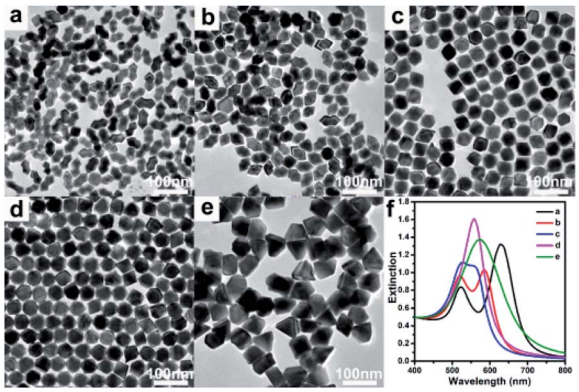

Fig. 2 TEM images (a to e) and UV-vis spectra (f) of Au@AuAg NPs synthesized at different volume of the as-prepared Au NR seed solutions in the growth solution: (a) 900, (b) 600, (c) 450, (d) 300, and (e) 100 μL. The concentrations of CTAC, $HAuCl_4$, $AgNO_3$, and AA are 33.3, 0.24, 0.1, and 1.44 mM, respectively.

led to various morphologies, including octahedrons, truncated tetrahedrons, and tetrahedrons (Fig. 2e).

Each product exhibits distinct plasmonic features in the UV-vis spectra (Fig. 2f), demonstrate that various nanostructures were formed at different volumes of the Au NRs, which was also confirmed by TEM characterization (Fig. 2a–e). The arrow-head shaped NPs display two individual SPR peaks, a L-SPR peak centered at 630 nm and a weak T-SPR peak at 523 nm. When the Au NR volume was decreased to 600 μL, the L-SPR peak blue-shifted to 585 nm, while the T-SPR peak red-shifted to 520 nm with a significantly stronger in intensity largely which may be attributed to the increase in the NPs lateral dimensions. When the Au NR volume was decreased to 400 μL, reduction in aspect ratio led to the L-SPR peak continue blue-shifted to 556 nm and the T-SPR peak red-shifted to 526 nm, while the T-SPR peak became even stronger than the L-SPR peak. Upon the formation of concave octahedral NPs, the two peaks merge into a single peak centered at 558 nm. Gradually, that peak subsequently undergoes a red-shift because of the increase in size. This results demonstrate that the shape of products and the corresponding L-SPR spectrum could be easily regulated under identical experimental conditions (*i.e.*, $HAuCl_4$, $AgNO_3$, AA, and CTAC concentrations) except for varying the amount of seed (Au NR).

The role of each reactant in the growth process is further determined by carefully modifying the reaction conditions and tracking the shape evolution process. The morphologies and spectra of the products can be controlled by changing the concentration of Au precursor in the growth solution under the same experimental conditions. Fig. 3 shows the TEM images and UV-vis spectra of a series of products obtained under the condition of increasing $HAuCl_4$ concentration while keeping the $HAuCl_4$ to AA ratio, Ag^+ ions, Au NR seed, and CTAC concentrations constant. Well-defined arrow-shaped Au NPs (Fig. 3a) were synthesized at lower $HAuCl_4$ concentrations of 0.083 mM, indicates that the two ends of Au NR grow preferentially under the condition of low Au^{3+} concentration. When

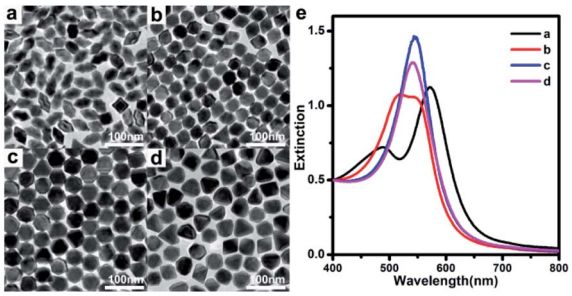

Fig. 3 TEM images (a to d) and UV-vis spectra (e) of Au@AuAg NPs synthesized at different $HAuCl_4$ concentrations: 0.083 (a), 0.167 (b), 0.24 (c), and 0.42 mM (d). The volume of as-prepared Au NR solutions is 300 μL. The concentrations of CTAC and $AgNO_3$ are 33.3 mM and 100 μM, respectively. The ratios of AA to $HAuCl_4$ in all experiments are kept as 6 : 1.

the concentrations of $HAuCl_4$ increased to 0.167 mM, arrow-shaped gradually disappears while spindle shaped and a small number of concave octahedral Au NPs were obtained (Fig. 3b). The L-SPR peak and T-SPR peak have a tendency to merge into one corresponds to the decrease of the aspect ratio in conformance with the TEM result, indicating the favorable deposition at the side of the Au NR. When the concentration of $HAuCl_4$ was 0.24 mM, concave octahedral Au NPs were obtained (Fig. 3c) and mainly one peak at 574 nm dominates. Additionally, further increasing $HAuCl_4$ concentration to 0.42 mM, tetrahedral Au NPs were formed (Fig. 3d). Investigated by EDS analysis, the results show that the Au/Ag atomic ratio of the as-prepared NPs were 61.2/38.8, 70.5/29.5, 75.3/24.7, 81.7/18.3, respectively (Table S1†).

The role of the silver on the overgrowth of Au NR was investigated by varying the $AgNO_3$ concentration from 33 to 167 μM. The TEM images in Fig. 4 reveal the shape evolution of NPs along with increasing $AgNO_3$ concentration. At a lower $AgNO_3$ concentration (33 μM), the shape of the NPs was transformed from original NR to spindle shaped NPs (Fig. 4a), suggesting that the atoms prefer deposited at the tips of NRs. As the concentration of $AgNO_3$ increased to 66 μM, the product becomes irregularly shaped NPs (Fig. 4b). When the $AgNO_3$ concentration was 100 μM, concaved octahedral Au@AuAg NPs were obtained (Fig. 3c). Continue to increase $AgNO_3$ concentration, the product transformed into a slightly truncated concave octahedron (Fig. 4c and d). The UV-vis spectra (Fig. 4e) of the samples show that the SPR band first narrowed and then red-shifted from 538 to 553 nm, which is consistent with the shape evolution seen in the TEM images. The Au/Ag atomic ratio of the as-prepared NPs are 89.3/10.7, 83.6/16.5, 69.3/30.7, 62.0/38.0, respectively, according to the EDS results (Table S2†). The abovementioned results show that adjusting the molar ratio of the Au and Ag precursors added in the overgrowth solution can regulate the elemental composition ratio of the product, and has an important influence on their morphological changes.

We further explore the effect of CTAC concentration on the construction of concave octahedral Au@AuAg NPs (Fig. S3†). Au@AuAg NPs with concave octahedral structure can be obtained at low CTAC concentration (0.008–0.033 M), while at high CTAC concentration (>0.067 M), the NPs are passivated to form smooth angles and the concave structure gradually disappeared. Based on the above experimental results, the major factors for the morphology regulation are Au NR seeds, $HAuCl_4$ and $AgNO_3$ precursor in the reaction process.

The composition of the resulting concave octahedral Au@AuAg NPs was investigated by HAADF-STEM image and the corresponding EDS related elemental mapping. Fig. 5a shows a typical HDAAF-STEM image taken from an individual concave octahedral Au@AuAg NP. The corresponding related elemental mappings (Fig. 5b–d) clearly reveal the spatial distributions of Au (red) and Ag (green), suggesting that Au and Ag atoms were uniformly mixed in the shell. This conclusion was further confirmed by the cross-sectional compositional line profile result (Fig. 5e), where Au and Ag signals occurred concomitantly during electron beam scanning across the concave octahedral NP. The EDS spectrum of the concave octahedral Au@AuAg NPs (Fig. S4†) further confirms that the concave octahedral Au@AuAg NPs are composed of Au and Ag. Based on the EDS results, the Ag atomic fraction is approximately 25%, which is consistent with the molar ratio of Au (including $HAuCl_4$ and Au NRs) and Ag added to the growing solution.

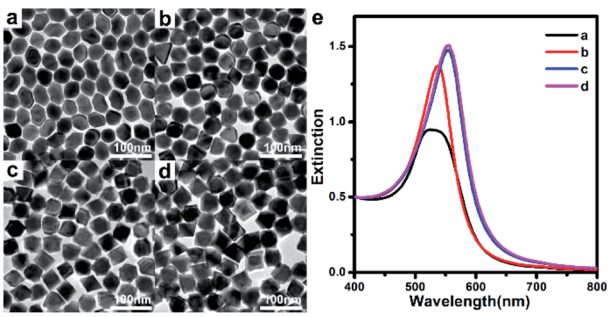

Fig. 4 TEM images (a to d) and UV-vis spectra (e) of Au@AuAg NPs synthesized at different $AgNO_3$ concentrations: 33 μM (a), 66 μM (b), 132 μM (c), and 167 μM (d). The volume of as-prepared Au NR solutions in the growth solution is 300 μL. The concentrations of CTAC, $HAuCl_4$, and AA in the growth solution are 0.03 M, 0.24 mM, and 1.44 mM, respectively.

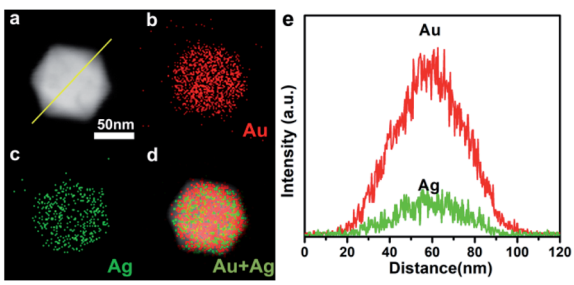

Fig. 5 HAADF-STEM image (a), EDS elemental mapping images of Au and Ag (b and c), and their overlapped image (d), and cross-sectional compositional line profile (e) of an individual concave octahedral Au@AuAg NP.

Furthermore, the intrinsic alloy properties of the prepared concave octahedral Au@AuAg NPs were characterized by XRD. As seen from the XRD spectra (Fig. S5†), several characteristic diffraction peaks of concave octahedral Au@AuAg NPs were indexed as the (111), (200), (220), (311), and (222) planes of a face-center-cubic (fcc) lattice.[40] Their peaks are located between the standard diffraction peaks of the fcc structure of pure Au (JCPDS no. 04-0784) and pure Ag (JCPDS no. 46-1043). However, since the lattice spacing of pure Au and pure Ag is very close, only in the diffraction at higher 2θ values was observed a slight shift and the peak positions centered at 64.53°, 77.53°, and 81.63° lie between the positions of pure Au (64.58°, 77.55°, and 81.72°) and pure Ag (64.43°, 77.47°, and 81.54°), suggested the formation of the AuAg alloy structure.[41]

A simple bulk solvent evaporation strategy was used to realize the self-assembly of concave octahedral Au@AuAg NPs into a large-area ordered structures. After evaporation of solvents, the as-prepared monodisperse concave octahedral Au@AuAg NPs easily to form an ordered array by uniform deposition on the glass sheet, forming a mirror-like metallic luster film (Fig. S6a†). This strategy avoids the coffee ring effect and the unrepeatability problem, which caused by uncontrollable factors in the process of NP aggregation during the simple drop coating deposition method, favors the distribution of NPs on the substrate more homogeneous. Besides, the assembly of concave octahedral Au@AuAg NPs on a glass sheet was characterized by SEM images, as shown in Fig. S6b.† Notably, the concave octahedral Au@AuAg NPs were uniformly distributed on the substrate without agglomeration and display a loosely hexagonal close-packed arrangement (inset in Fig. S6b†), which can act as effective hotspots for SERS. In consequence, it provides a precondition for the good uniformity of concave octahedral Au@AuAg NP ordered array as SERS substrates.

The SERS performances of as-prepared concave octahedral Au@AuAg NPs assembly were explored by using R6G as probe molecule under 633 nm excitation. For comparison, the SERS spectra of R6G absorbed on octahedral Au NPs (Fig. S7†) without a concave structure and AuAg bimetallic shell and 50 nm Ag NPs (Fig. S8†) were recorded (Fig. 6a). Several Raman characteristic peaks of the R6G molecule appeared at *ca.* 613, 775, 1180, 1310, 1362, 1510, 1574, and 1650 cm^{-1} are presented in Fig. 6a, which are in good agreement with those that have been obtained in the literature.[42–46] The intense SERS signals at about 613, 775 and 1180 cm^{-1} are attributed to the C–C–C ring in-plane vibration mode, the C–H out-of-plane bending mode and the C–H in-plane bending mode of the R6G molecule, respectively. In addition, the peaks at the wavenumbers of about 1310 cm^{-1} correspond to C–O–C stretching mode while those at 1365, 1510, and 1650 cm^{-1} were caused by the totally symmetric mode of in plane C–C stretching vibration. Compared with octahedral Au NPs substrates, the concave octahedral Au@AuAg NPs and Ag NPs substrates exhibited much stronger and better resolved spectra for R6G. In addition, the SERS performance of the concave octahedral Au@AuAg NPs also higher than that of Ag NPs. This Raman enhancement can be mainly attributed to the local electric field enhancement generated by edges and corners of the unique concave structure and the presence of AuAg bimetallic shell.

To better ascertain the enhancement sensitivity of the prepared concave octahedral Au@AuAg NPs, we recorded the SERS spectra of R6G with various concentrations in a range of 10^{-4} to 10^{-10} M. In the corresponding SERS spectra (Fig. 6b), we can clearly observe that the intensity of Raman signal decreases gradually with the decrease of R6G concentration. Notably, five well-resolved Raman signals of R6G at 610, 775, 1310, 1362, and 1510 cm^{-1} can be still clearly detectable even when the R6G was reduced to an ultralow concentration of 10^{-10} M. Therefore, their detection limits for R6G can reach to a concentration as low as 10^{-10} M, further confirming the concave octahedral Au@AuAg NPs substrate are excellent SERS sensitivity. Additionally, as described in the ESI,† the SERS enhancement factor (EF) of the concave octahedral Au@AuAg NPs SERS substrate were evaluated to be 1.3×10^7 under the 10^{-8} M R6G solution of SERS and 10^{-2} M R6G solution of normal Raman experiment (Fig. S9†), revealing an excellent enhanced performance of the concave octahedral Au@AuAg NPs array owing to their abundant hotspots.[47,48] The EF of the concave octahedral Au@AuAg NPs was much larger than many earlier reports with respect to Au@Ag NPs (EF = 1.02×10^7),[49] porous Au–Ag hybrid nanoplates (EF = 1.4×10^6),[50] and nanosponges (EF = 6.4×10^5).[51]

In practical applications, with the exception of the high SERS enhancement ability and sensitivity, the uniformity and reproducibility of Raman signals are also two crucial factors for an excellent SERS substrate. To investigating the uniformity and reproducibility of the concave octahedral Au@AuAg NPs structure, 10 arbitrarily selected spots on the substrates were used for the SERS test of R6G (10^{-6} M). The corresponding SERS signals intensity of the 613 cm^{-1} peak (Fig. 7a) demonstrating good signal uniformity and reproducibility of the SERS substrate when examined upon the entire surface. Furthermore, we also compared the intensities of the 613 cm^{-1} peak of R6G, and the relative standard deviation (RSD) value was calculated to be about 8.3%, which indicated the high uniformity and reproducibility of the SERS performance (Fig. 7b). The high repeatability of SERS performance can be reasonably attributed to the uniform distribution of NPs on the glass.

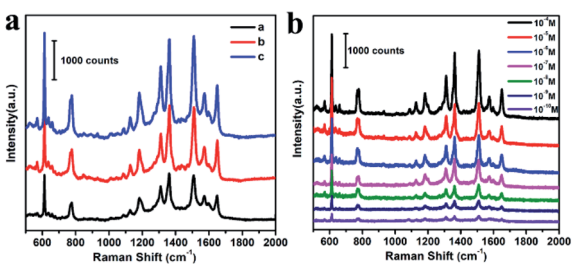

Fig. 6 (a) SERS spectra of R6G molecules (0.1 mM) absorbed on the aggregates of corresponding octahedral Au NPs (black line), Ag NPs (red line) and concave octahedral Au@AuAg NPs (blue line) on glass substrates. (b) SERS spectra of different concentrations of R6G molecule (from 10^{-4} to 10^{-10} M) on the concave octahedral Au@AuAg NPs. The excitation laser wavelength for Raman measurements is 633 nm, the laser power is 0.2 mW, and the acquisition time is 10 s.

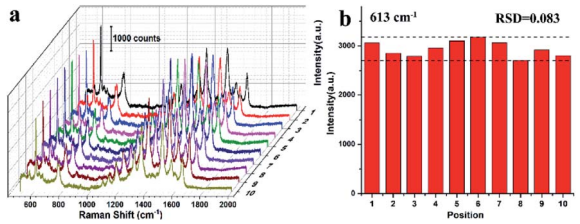

Fig. 7 The Raman spectra of R6G molecule collected at 10 arbitrarily selected spots from concave octahedral Au@AuAg NPs substrates (a). The histogram characterization of the intensities at the 613 cm^{-1} peak derived from the Raman spectra (b).

4. Conclusions

In summary, a well-designed concave octahedral Au@AuAg NPs were synthesized *via* epitaxial growth of Au and Ag on the Au NRs. The final Au@AuAg NPs with a fascinating concave geometry structure and AuAg alloy shell. By tracking the growth process and recording the shape evolution process, we demonstrate pivotal roles of both the concentration of additives (including Au NR seeds, $HAuCl_4$, and $AgNO_3$ precursor) and reaction time in exquisitely tuning crystal growth of concave octahedral Au@AuAg NPs. The obtained NPs show adjustable distinct plasmonic properties. Further, we utilized these NPs as SERS substrate to detect target analyte, R6G, where the concave octahedral Au@AuAg NPs were found exhibit higher SERS activity than octahedral Au NPs with comparable sizes, made possible by the incorporation of AuAg shell and distinct concave structure. Furthermore, the concave octahedral Au@AuAg NPs exhibit an EF of 1.3×10^7 and a low detection limit of 10^{-10} M arises from the synergistic effect between Au and Ag elements and concave structure. In addition to higher sensitivity and low detection limit, the obtained SERS substrate exhibits excellent signal uniformity and repeatability (RSD $\approx$ 8.3%) due to its highly ordered array structures on a large area. This work opens a new avenue toward bimetallic NPs with concave structure, which has broad application prospect in optics, SERS detection and other fields.

Conflicts of interest

There are no conflicts to declare.

Acknowledgements

This work is financially supported by the Natural Science Foundation of China (Grant no. 52101227, 11904197), Shandong Provincial Natural Science Foundation (ZR2020QE005), and Qufu Normal University for a scientific research foundation (107/613901).

References

1 S. Schlücker, *Angew. Chem., Int. Ed.*, 2014, **53**, 4756–4795.
2 P. Ye, W. Xin, I. M. De Rosa, Y. Wang, M. S. Goorsky, L. Zheng, X. Yin and Y. H. Xie, *ACS Appl. Mater. Interfaces*, 2020, **12**, 22050–22057.
3 M. J. Mulvihill, X. Y. Ling, J. Henzie and P. Yang, *J. Am. Chem. Soc.*, 2010, **132**, 268–274.
4 T. Zheng, G. G. Li, F. Zhou, R. Wu, J. J. Zhu and H. Wang, *Adv. Mater.*, 2016, **28**, 8218–8226.
5 E. Y. Ye, M. D. Regulacio, S. Y. Zhang, X. J. Loh and M. Y. Han, *Chem. Soc. Rev.*, 2015, **44**, 6001–6017.
6 H. D. Yu, M. D. Regulacio, E. Y. Ye and M. Y. Han, *Chem. Soc. Rev.*, 2013, **42**, 6006–6018.
7 H. K. Lee, Y. H. Lee, C. S. L. Koh, G. C. Phan-Quang, X. Han, C. L. Lay, H. Y. F. Sim, Y.-C. Kao, Q. An and X. Y. Ling, *Chem. Soc. Rev.*, 2019, **48**, 731–756.
8 W. Kim, S. H. Lee, J. H. Kim, Y. J. Ahn, Y.-H. Kim, J. S. Yu and S. Choi, *ACS Nano*, 2018, **12**, 7100–7108.
9 C. Zhu, G. Meng, P. Zheng, Q. Huang, Z. Li, X. Hu, X. Wang, Z. Huang, F. Li and N. Wu, *Adv. Mater.*, 2016, **28**, 4871–4876.
10 S. Bai, D. Serien, A. Hu and K. Sugioka, *Adv. Funct. Mater.*, 2018, **28**, 1706262.
11 S. Ben-Jaber, W. J. Peveler, R. Quesada-Cabrera, E. Cortés, C. Sotelo-Vazquez, N. Abdul-Karim, S. A. Maier and I. P. Parkin, *Nat. Commun.*, 2016, **7**, 12189.
12 X. Wang and L. Guo, *Angew. Chem., Int. Ed.*, 2020, **59**, 4231–4239.
13 J. Kim, C. Lee, Y. Lee, J. Lee, S. Park, S. Park and J. Nam, *Adv. Mater.*, 2021, **33**, 2006966.
14 J. Reguera, J. Langer, D. Jiménez de Aberasturi and L. M. Liz-Marzán, *Chem. Soc. Rev.*, 2017, **46**, 3866–3885.
15 H. Tian, H. Li and Y. Fang, *ACS Appl. Mater. Interfaces*, 2019, **11**, 16207–16213.
16 M. Rycenga, C. M. Cobley, J. Zeng, W. Li, C. H. Moran, Q. Zhang, D. Qin and Y. Xia, *Chem. Rev.*, 2011, **111**, 3669–3712.
17 X. Zhu, X. Zhuo, Q. Li, Z. Yang and J. Wang, *Adv. Funct. Mater.*, 2016, **26**, 341–352.
18 Y. Zheng, J. Zeng, A. Ruditskiy, M. Liu and Y. Xia, *Chem. Mater.*, 2014, **26**, 22–33.
19 S. Eustis and M. A. El-Sayed, *Chem. Soc. Rev.*, 2006, **35**, 209–217.
20 Y. Liu, J. Zhou, B. Wang, T. Jiang, H.-P. Ho, L. Petti and P. Mormile, *Phys. Chem. Chem. Phys.*, 2015, **17**, 6819–6826.
21 Y. Yang, J. Liu, Z. Fu and D. Qin, *J. Am. Chem. Soc.*, 2014, **136**, 8153–8156.
22 Z. Zhao, Y. Huang, Y. Fan and K. Lai, *Nanomaterials*, 2018, **8**, 94.
23 Z. Huang, G. Meng, X. Hu, Q. Pan, D. Huo, H. Zhou, Y. Ke and N. Wu, *Nano Res.*, 2019, **12**, 449–455.
24 J. Ahn, D. Wang, Y. Ding, J. Zhang and D. Qin, *ACS Nano*, 2018, **12**, 298–307.
25 H. Lv, L. Sun, J. Feng, J. Na, D. Xu, Y. Yamauchi and B. Liu, *Chem. Commun.*, 2020, **56**, 9679–9682.
26 C. Hao, L. Xu, M. Sun, W. Ma, H. Kuang and C. Xu, *Adv. Funct. Mater.*, 2018, **28**, 1802372.
27 L. Dai, L. Song, Y. Huang, L. Zhang, X. Lu, J. Zhang and T. Chen, *Langmuir*, 2017, **33**, 5378–5384.

28 J. Zhang, M. R. Langille, M. L. Personick, K. Zhang, S. Li and C. A. Mirkin, *J. Am. Chem. Soc.*, 2010, **132**, 14012–14014.
29 X. Xia, J. Zeng, B. McDearmon, Y. Zheng, Q. Li and Y. Xia, *Angew. Chem., Int. Ed.*, 2011, **50**, 12542–12546.
30 L. Li, Y. Peng, Y. Yue, Y. Hu, X. Liang, P. Yin and L. Guo, *Chem. Commun.*, 2015, **51**, 11591–11594.
31 M. Rycenga, M. R. Langille, M. L. Personick, T. Ozel and C. A. Mirkin, *Nano Lett*, 2012, **12**, 6218–6222.
32 A. Maiti, A. Maity, B. Satpati, N. Large and T. K. Chini, *J. Phys. Chem. C*, 2017, **121**, 731–740.
33 Y. Huang, L. Wu, X. Chen, P. Bai and D.-H. Kim, *Chem. Mater.*, 2013, **25**, 2470–2475.
34 X. Xia, J. Zeng, B. McDearmon, Y. Zheng, Q. Li and Y. Xia, *Angew. Chem., Int. Ed.*, 2011, **50**, 12542–12546.
35 M. Rycenga, M. R. Langille, M. L. Personick, T. Ozel and C. A. Mirkin, *Nano Lett*, 2012, **12**, 6218–6222.
36 J. Ahn, D. Wang, Y. Ding, J. Zhang and D. Qin, *ACS Nano*, 2018, **12**, 298–307.
37 B. Nikoobakht and M. A. El-Sayed, *Chem. Mater.*, 2003, **15**, 1957–1962.
38 C. Bi, Y. Song, H. Zhao and G. Liu, *ACS Appl. Nano Mater.*, 2021, **4**, 4584–4592.
39 Q. Wang, Z. Wang, Z. Li, J. Xiao, H. Shan, Z. Fang and L. Qi, *Sci. Adv.*, 2017, **3**, e1701183.
40 J. Yan, X. Han, J. He, L. Kang, B. Zhang, Y. Du, H. Zhao, C. Dong, H.-L. Wang and P. Xu, *ACS Appl. Mater. Interfaces*, 2012, **4**, 2752–2756.
41 Q. Cao, K. Yuan, Q. Liu, C. Liang, X. Wang, Y.-F. Cheng, Q. Li, M. Wang and R. Che, *ACS Appl. Mater. Interfaces*, 2015, **7**, 18491–18500.
42 P. Hildebrandt and M. Stockburger, *J. Phys. Chem.*, 1984, **88**, 5935–5944.
43 J. Lee, J. Seo, D. Kim, S. Shin, S. Lee, C. Mahata, H. S. Lee, B.-W. Min and T. Lee, *ACS Appl. Mater. Interfaces*, 2014, **6**, 9053–9060.
44 S. Bai, D. Serien, A. Hu and K. Sugioka, *Adv. Funct. Mater.*, 2018, **28**, 1706262.
45 R. Contreras-Caceres, C. Dawson, P. Formanek, D. Fischer, F. Simon, A. Janke, P. Uhlmann and M. Stamm, *Chem. Mater.*, 2013, **25**, 158–169.
46 S. Nie and S. R. Emory, *Science*, 1997, **275**, 1102–1106.
47 E. C. Le Ru, E. Blackie, M. Meyer and P. G. Etchegoin, *J. Phys. Chem. C*, 2007, **111**, 13794–13803.
48 A. N. Severyukhina, B. V. Parakhonskiy, E. S. Prikhozhdenko, D. A. Gorin, G. B. Sukhorukov, H. Möhwald and A. M. Yashchenok, *ACS Appl. Mater. Interfaces*, 2015, **7**, 15466–15473.
49 K. Yuan, J. Zheng, D. Yang, B. J. Sanchez, X. Liu, X. Guo, C. Liu, N. E. Dina, J. Jian, Z. Bao, Z. Hu, Z. Liang, H. Zhou and Z. Jiang, *ACS Omega*, 2018, **3**, 2855–2864.
50 X. Wei, Q. Fan, H. Liu, Y. Bai, L. Zhang, H. Zheng, Y. Yin and C. Gao, *Nanoscale*, 2016, **8**, 15689–15695.
51 Y. Yan, A. I. Radu, W. Rao, H. Wang, G. Chen, K. Weber, D. Wang, D. Cialla-May, J. Popp and P. Schaaf, *Chem. Mater.*, 2016, **28**, 7673–7682.